scientific reports

OPEN

Fabrication of near-invisible solar cell with monolayer WS$_2$

Xing He, Yuta Iwamoto, Toshiro Kaneko & Toshiaki Kato✉

Herein, we developed a near-invisible solar cell through a precise control of the contact barrier between an indium tin oxide (ITO) electrode and a monolayer tungsten disulfide (WS$_2$), grown by chemical vapor deposition (CVD). The contact barrier between WS$_2$ and ITO was controlled by coating various thin metals on top of ITO (M$_x$/ITO) and inserting a thin layer of WO$_3$ between M$_x$/ITO and the monolayer WS$_2$, which resulted in a drastic increase in the Schottky barrier height (up to 220 meV); this could increase the efficiency of the charge carrier separation in our Schottky-type solar cell. The power conversion efficiency (PCE) of the solar cell with the optimized electrode (WO$_3$/M$_x$/ITO) was more than 1000 times that of a device using a normal ITO electrode. Large-scale fabrication of the solar cell was also investigated, which revealed that a simple size expansion with large WS$_2$ crystals and parallel long electrodes could not improve the total power (P$_T$) obtained from the complete device even with an increase in the device area; this can be explained by the percolation theory. This problem was addressed by reducing the aspect ratio (width/channel length) of the unit device structure to a value lower than a critical threshold. By repeating the experiments on this optimized unit device with an appropriate number of series and parallel connections, P$_T$ could be increased up to 420 pW from a 1-cm^2 solar cell with a very high value (79%) of average visible transmission (AVT).

Transparent solar cells (TSCs) have attracted considerable attention as they can overcome the limitations of traditional non-transparent solar cells[1], which can convert diverse components, such as architectural windows, agricultural sheds, glass panels of smart devices, and even human skin into energy harvesting devices. Despite the recent developments in TSCs with perovskite[2] and organic semiconductors[3–5], the average visible transparency (AVT) of these resources is lower than 70%; thus, TSCs with very high AVT values (> 70%), here we call "near invisible solar cells (NISCs)", is still challenging. To the best of our knowledge, NISCs have been realized only by combining several devices. Transparent luminescent solar concentrators (TLSCs)[6,7] absorb UV or IR and generate bright luminescence, which propagates to the edge of the TLSC by internal reflection. Electrical power generation can be achieved at the edge of the TLSCs using a conventional non-transparent Si solar cell, resulting in a very high AVT (> 80%). However, a non-transparent part is always required at the edge of the device, suggesting that scalability issues could arise[6,7]. Recently, TSCs with relatively high AVT values have been reported in AZO-embedded ZnO/NiO/AgNW[8] (70%), dye[9] (75%) and ClAlPc:C$_{60}$[10] (77.45%). These can be candidates of NISCs.

Two-dimensional (2D) transition metal dichalcogenides (TMDs), especially for monolayer- and few layered TMDs, including suitable band gaps in the visible light range and highest absorption co-efficiency per thickness[11,12], are considered to be one of the most promising materials for the fabrication of NISCs. To date, many TMD-based solar cells have been investigated by employing pn junctions[13–17], heterojunctions[18–20], Schottky junctions[21] etc. (Tables S1 and S2). However, most of them are non-transparent owing to the use of opaque Si substrates and non-transparent metal electrodes[13–17,19]. Even though devices of μm-scale can attain a certain power conversion efficiency (PCE), the total power (P$_T$) obtained from the whole device within the same substrate is too low to be applied[22,23] in devices because of their lack of scalability. In our previous study, a highest PCE of 0.7% was achieved using a triple-layer TMD[21] with a Schottky junction structure. This Schottky junction structure can be expanded and applied even on a polyethylene naphthalate (PEN) substrate at cm-scales. However, there was a trade-off between transparency and P$_T$ because non-transparent metal electrodes were utilized. Thus, transparent electrodes and monolayer TMDs should be employed to realize TMD-based NISCs with a relatively high P$_T$.

In this study, we successfully fabricated an NISC using ITO and monolayer tungsten disulfide (WS$_2$) as transparent electrodes, and photoactive layer, respectively. The contact issue between ITO and WS$_2$ was investigated, revealing that a pure ITO–WS$_2$ junction possessed a relatively low Schottky barrier height (Φ_B) (< 10 meV), and a thin Cu-coated ITO electrode with an insertion of WO$_3$ (WO$_3$/Cu/ITO) could increase Φ_B up to approximately 220 meV in contact with WS$_2$; this can be useful for carrier collection and generation within a Schottky-type solar cell, respectively. Furthermore, it was found that an appropriate architectural design would be vital to scale up the TMD-based solar cell to avoid an unexpected drop in the open circuit voltage (V$_{OC}$), which can be

Graduate School of Engineering, Tohoku University, Sendai 980-8579, Japan. ✉email: kato12@tohoku.ac.jp
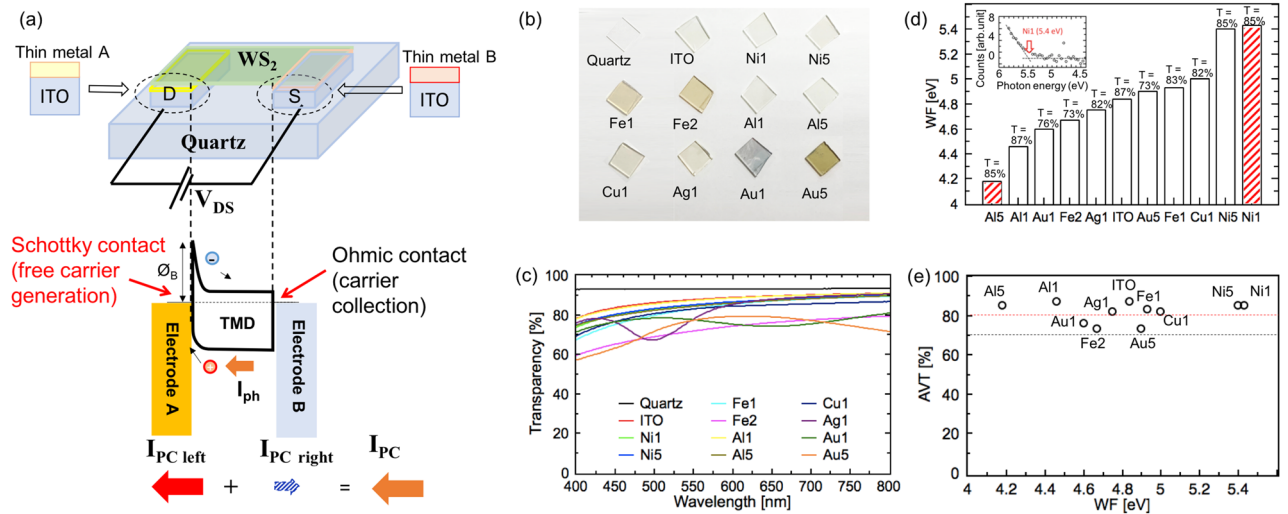
Figure 1. (**a**) Schematic illustration of device structure and ideal optimal band structure for the transparent Schottky solar cell. (**b**) Images of samples for WF and AVT measurement. ITO was sputtered on quartz substrate and a thin metal film was coated on the top of ITO. (**c**) Transparency spectra of quartz, ITO/quartz, and Mx/ITO on quartz (Mx = Ni1, Ni5, Fe1, Fe2, Al1, Al5, Cu1, Ag1, Au1, and Au5). (**d**) Plot of WF for Mx/ITO measured by PYS. Inset in (**d**) shows typical photoemission features of Ni1/ITO and fitting curve to obtain the WF. (**e**) Scatters of transparency and work function of tested Mx/ITO.

overcome by controlling the aspect ratio of the unit device. It was demonstrated that P_T could reach up to 420 pW from a 1-cm^2 device with a high AVT of 79%; thus, the fabrication of NISC was first realized by using TMD.

Results and discussion

Work function control of ITO. The device structure and ideal band structure of the Schottky-type solar cell are shown in Fig. 1a. The discrepancy in the work function (WF) between electrode A and the semiconductor produces a built-in potential, which separates the photogenerated electron–hole pairs. Once the generated carriers travel to the opposite electrode, power generation can be realized. In our previous study, it was proven that the greater the WF difference between the asymmetric electrodes, the higher the resultant PCE; this is consistent with this power generation model. Thus, in this study, the WF control of ITO was the first objective towards obtaining an optimal band structure for the Schottky-type solar cell. Regarding to the interface, it should be notice that, it is better to avoid other interface impurity, because sometimes it could affect the interface charge and energy distribution that lead to some undesired surface recombination, reducing the separation efficiency of carriers at the interface barrier, thereby reducing the V_{OC}.

To modulate the WF, different types of thin metal films were coated on ITO. After an Mx coating (Fig. 1b, c; M is a metal and x is thickness in nm), some Mx/ITOs can maintain a high AVT of greater than 80%, such as Ni1, Ni5, Fe1, Al1, Al5, Cu1, and Ag1; this indicates their potential to be used as electrodes in TSCs. The WF of the Mx/ITO was then measured using photoelectron yield spectroscopy (PYS). It was found that the WF of the Mx/ITO varied in the range of 4.2– 5.4 eV (Fig. 1d). Moreover, most of them had a transparency of more than 80%, indicating that the WF of ITO was successfully modulated by maintaining the original high transparency of ITO (Fig. 1e). As a monolayer WS$_2$ grown by CVD is naturally n-doped by impurities and the WF is measured to be around 4.9 eV, Mx/ITOs with WF higher and lower than 4.9 eV are promising candidates as transparent electrode with Schottky contacts (Ni1, Ni5, Cu1 and Fe1), and Ohmic-like contacts (Al5, Al1, Ag1, ITO), respectively against a monolayer WS$_2$.

Schottky barrier height measurement and control. The purpose of controlling the WF was to control Φ_B in both the contacts. Thus, it is important to understand the band structure of a real device. Here, the spatially resolved photoexcited charge-carrier mapping (SPCM) method was used to measure the potential profile of the real device[24]. By using this method, the detailed band structure between the Mx/ITO and TMD could be obtained under the ambient condition, which is the operating condition of the solar cell. The monolayer WS$_2$ was used as the photoactive channel material in contact with Cu/ITO (left) and Ni/ITO (right) (Fig. 2a and b). The methodology to obtain the potential profile is outlined below: (1) A 633 nm cw excitation light was delivered by a 100 objective (laser spot size ~ 1um) and focused on the sample to be scanned over the samples (electrode width ~ 2um, channel length > 3um) in a form of line/fixed position. A line scan from the drain to source electrode, that is, from Point A to Point B was taken, measuring all the spots within this scan. Synchronous detection of photocurrent (the source-drain current (I_{DS})) was achieved (Fig. 2c); (2) I_{DS} was integrated from Point A to B (Drain to Source) (Fig. 2d, black line); (3) The y-axis was switched to present the electron negative potential (potential A is always zero) (Fig. 2d, red line), which could be considered to be the same as that of the conduction band (Fig. 2g) because of the simple approximation between the potential and carrier generation[24].
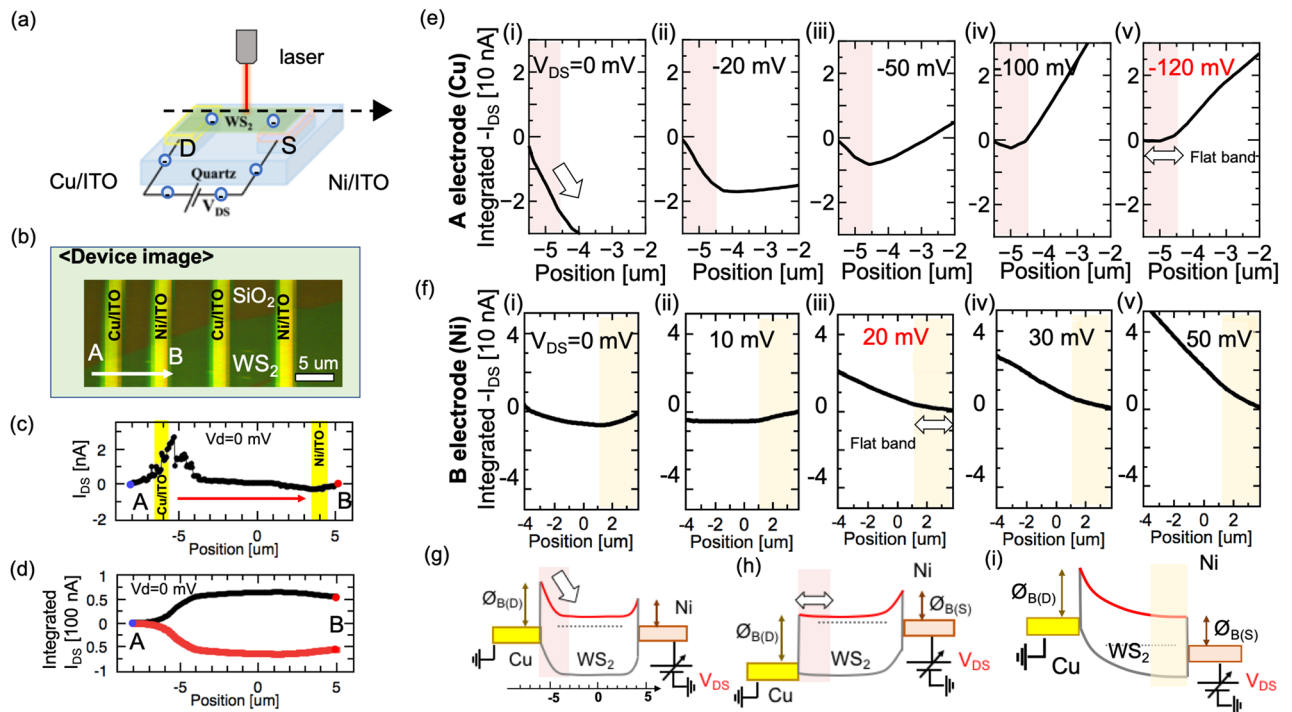
Figure 2. (**a**) Schematic illustration of spatially resolved photoexcited charge-carrier mapping for the device with asymmetric electrodes: Cu/ITO and Ni/ITO. (**b**) Images of the device under a microscope. (**c**) Photocurrent line scan of the device. (**d**) Integrated photocurrent based on photocurrent in (**c**) as the black line; the red line comes from inverse treatment of the y-axis, which represents the potential profile in the conduction band as shown in (**g**). (**e**), (**f**) (i–v) Profile of integrated I_{DS} at (**e**) Cu/ITO and (**f**) Ni/ITO side under different values of V_{DS}, respectively. (**g**)–(**i**) Typical band structure of (**g**) original and flat band in (**h**) Cu and (**i**) Ni side.

First, we focused on the Cu/ITO side under different source-drain bias voltages (V_{DS}) (Fig. 2e (i)–(v)). The negative slope of the potential near the Cu/ITO interface decreased with increasing V_{DS} and became almost flat at 120 mV, indicating that Φ_B at the Cu/ITO side was approximately 120 meV (Fig. 2h). Then, the slope changed from positive to negative slope at approximately 20 mV at the Ni/ITO side (Fig. 2f (i)–(v)), indicating that Φ_B on the Ni/ITO side was approximately 20 meV (Fig. 2i). Using the SPCM method, different types of Mx/ITO devices were systematically measured, and each Φ_B was carefully estimated from the V_{DS} dependency of the SPCM (Table S3). The correlation between Φ_B and the WF for different Mx/ITO interfaces is displayed in Fig. 3a. Several sets of devices tested and error bars are added (Fig. S1). It was found that all the data points except those for Ni followed a linear tendency in that Φ_B was proportional to the WF following the equation $\Phi_B = S_F \times (\Phi_m - \chi)$, where S_F, Φ_m, and χ are Fermi level pinning (FLP) factor, the WF of the conductive material and electron affinity of the semiconductor, respectively. Through curve-fitting our data using this formula, S_F was calculated to be approximately 0.25 (blue dashed line in Fig. 3a), which was consistent with the results for non-transparent bulk metal contact against TMDs obtained by other groups ($S_F = 0.1$–0.3)[25,26]. According to this equation, Φ_B of Ni should be approximately 200 meV, which is completely different from the experimental results ($\Phi_B = 10$–110 meV). It is known that metals with stronger/weaker binding energies (E_b) owing to their shorter/longer bonding distances (d) are considered to cause a stronger/weaker FLP effect[27]. Based on the previous theoretical calculation of the binding energy against TMDs, the E_b of Ni was obtained to be 510 meV, which was much higher than that of Cu (400 meV), Ag (350 meV), and Au (300 meV)[27], thus denoting a stronger FLP effect of Ni as compared to Cu, Ag, and Au. This relatively stronger FLP effect may account for the much lower Φ_B than the theoretical value for Ni.

Based on the above, it can be hypothesized that a slight increase/decrease in d (E_b) could weaken the FLP effect and increase Φ_B, resulting in an improved performance of the Schottky-type solar cell. To confirm this hypothesis, a thin WO_3 (a few nm) layer was inserted as an insulating oxide layer. WO_3 is a promising insulating material with high work function, good hole mobility and high transparency[28–30] were used as a interlayer between metal and semiconductor, to improve contact[31] and device performance, such as work as a buffer layer in photovoltaic devices[10,28] and improve the performance of transparent organic light emitting diode[32]. The WO_3 layer can be deposited by thermal evaporation, which is compatible to thermal evaporation of anode Au or Ag.

As a result, Φ_B of WO_3/Cu/ITO increased up to 220 meV (Fig. S2), which was much higher than that of Cu/ITO ($\Phi_B = 120$ meV) (Fig. 3a); this confirms the significant effect of WO_3 insertion on Φ_B. The S_F of WO_3/Cu/ITO was calculated to be approximately 0.56, which indicates a weakening of the FLP effect. There is also a possibility that WO_3 provides a carrier filtering effect and thus affects the performance of solar cells. Other oxide films and film thicknesses will be tried and clarified in the future.
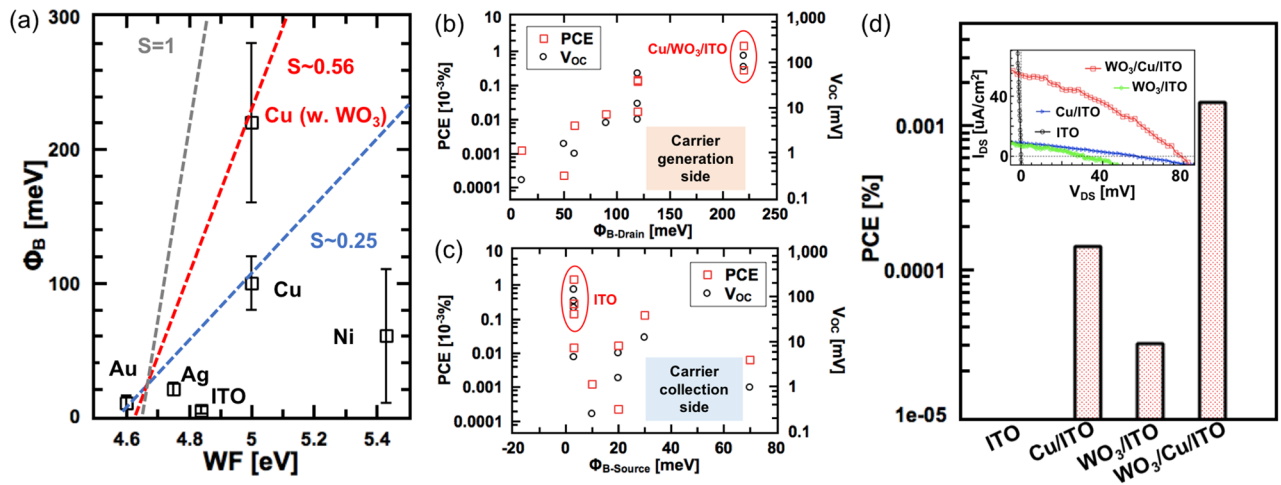
Figure 3. (**a**) Experimentally determined Schottky barrier height vs WF for different metal coated ITO with or without WO_3. Dashed lines represent theoretical calculations with different value of S (gray: S = 1, red: S = 0.56, blue: S = 0.25). (**b**), (**c**) Power conversion efficiency and open circuit voltage vs Schottky barrier height in the contact of (**b**) drain side and (**c**) source side. (**d**) PCE of different transparent Schottky solar cells fabricated by different kinds of symmetric or asymmetric electrodes. Insert in (**d**) is the typical I_{DS}-V_{DS} curve of these solar cells.

Because it is now possible to control Φ_B by tuning the surface of the ITO electrode, the PCE of our solar cell devices could be measured. The relationship between Φ_B and PCE is summarized in Fig. 3b, c. The PCE and V_{OC} increased with Φ_B at the drain side ($\Phi_{B\text{-drain}}$) (Fig. 3b), and decreased with Φ_B at the source side ($\Phi_{B\text{-source}}$) (Fig. 3c); this suggested that the higher PCE and V_{OC} originated from the higher $\Phi_{B\text{-drain}}$ and lower $\Phi_{B\text{-source}}$. Because the drain and source electrodes were designed for carrier generation and collection electrode of the Schottky-type solar cell, these results agreed well with those of our power generation model. Among these solar cells, WO_3/Cu/ITO with the highest $\Phi_{B\text{-drain}}$ exhibited the best PCE (1.45×10^{-3}%), which was 10 times higher than that of Cu/ITO (1.44×10^{-4}%), and more than 1000 times that of pure ITO (Fig. 3d) (Fig. S3).

Scale-up of highly transparent Schottky solar cells. Even though a very high PCE could be obtained from a small device at a μm-scale, the P_T of the entire device would be considerably limited by the device size. Thus, P_T is an important parameter for determining the potential of a solar cell for practical applications. As the solar cell study using TMDs is in a relatively nascent phase, P_T has not been discussed till date. In this study, we attempted to increase P_T to a practical level (more than 100 pW)[23] by scaling up the device. However, it can be seen that scaling up by increasing the channel width and number of parallel connections cannot effectively increase P_T, and may sometimes cause the P_T to drop instead (Fig. S4), indicating that it is necessary to choose a suitable architectural design to scale up the TMD-based solar cells. Here, some concrete strategies adopted for the scale-up include (1) designing the structure of the unit device (UD); (2) exploring parallel connections (named as unit module A (UDM-A)); (3) investigating series connections (named as unit device module B (UDM-B)); and (4) combining parallel and series connections (named as unit device module C (UDM-C)). The optimization of the architecture of each device is vital.

As a first step in designing a unit device (UD) structure, solar cells with various widths (W) and channel lengths (L_{ch}) were fabricated (Fig. 4a, b). The performance of the Schottky-type solar cells has been mainly discussed in terms of three aspects: P_T, V_{OC}, and short circuit current (I_{SC}). When $L_{ch} = 1$ μm, P_T increased with W up to 33.5 μm (Fig. 4c). However, when W was larger than 33.5 μm, P_T significantly decreased with W, that is, there was a threshold value of the critical width (W_{th}) essential to maintain a high P_T. The drop in P_T was mainly owing to V_{OC} dropping (Fig. 4d, e). Coincidentally, a similar tendency was observed in the devices with $L_{ch} = 2, 3,$ and 4 μm, with different W_{th} values of 81.3, 116.3 and 142.0 μm, respectively. Interestingly, there was an approximately linear relationship between W_{th} and L_{ch} (Fig. 4f), indicating that the aspect ratio of the device (W/L_{ch}) was critical to designing large-scale solar cells with TMDs, and it should be lower than approximately 36. This could be explained by the decrease in the parallel resistance. The UD can be treated as a combination of several small channels connected in parallel, and each channel has a shunt resistance of $R_{sh}(i)$ ($i = 1, 2.., n$) (Fig. S5). The total shunt resistance ($R_{sh\text{-total}}$) would depend on the resistance of each channel ($1/R_{sh\text{-total}} = \Sigma(1/R_{sh}(i))$). If channel (i) contains a metal-like pass, $R_{sh}(i)$ would be very low, resulting in a low $R_{sh\text{-total}}$ and a low V_{OC}. Candidates that would cause a low $R_{sh}(i)$ are possibly impurities, such as the 1 T phase of TMD or other impurities existing in TMD, which are inevitably induced by chemical vapor deposition or mechanical exfoliation[33]. The presence of impurities leads to the formation of band tail localized states, thereafter, percolation transport would arise in 2D disordered materials with energy variations along the current-carrying path[34,35]. When W increased, the possibility that the unexpected metal-like pass involved within the photoactive channel would increase, resulting in a low $R_{sh\text{-total}}$; this is known as the percolation model[36,37], and can explain the existence of W_{th} and the linear
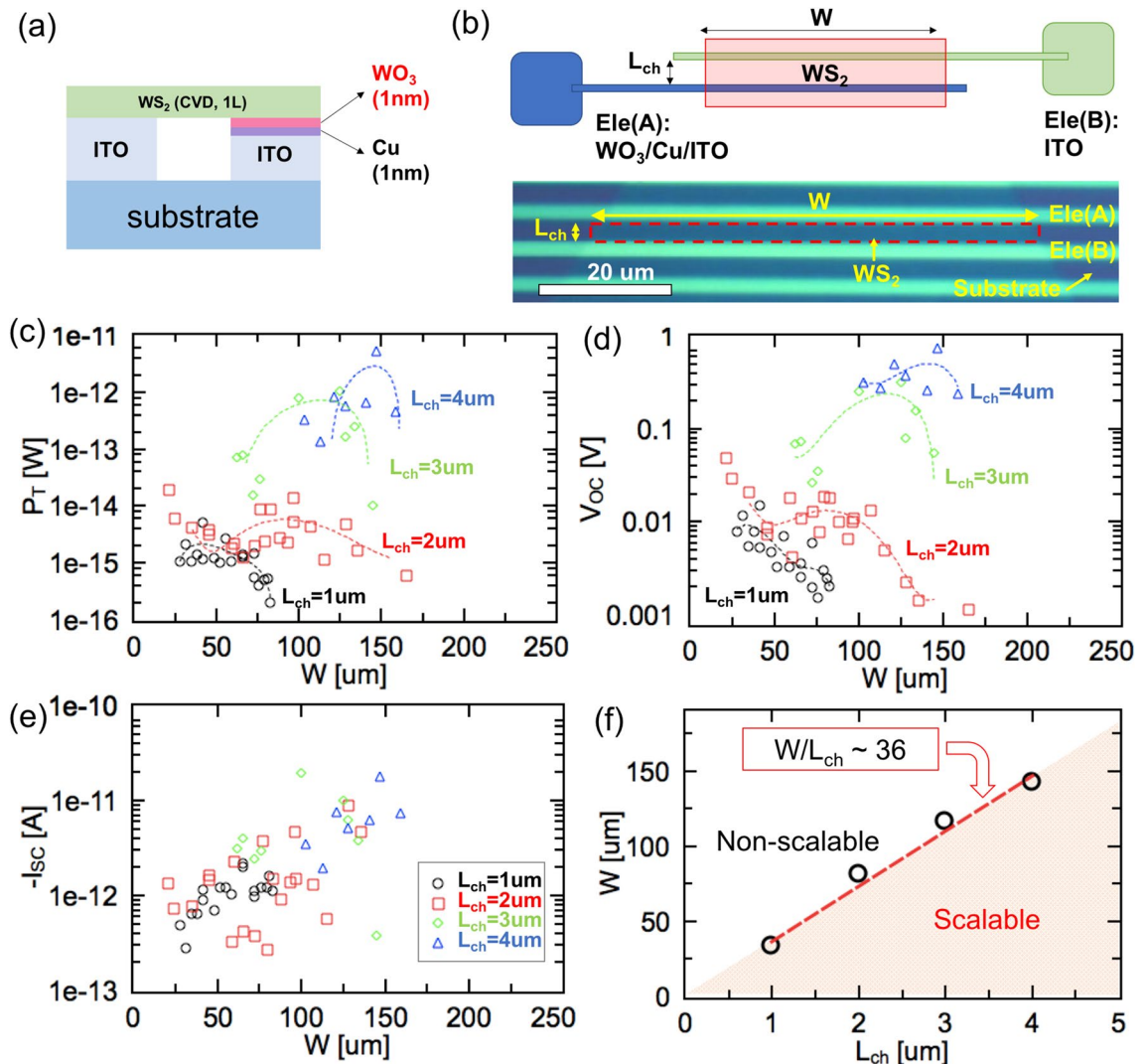
Figure 4. (**a**) Structure of devices used for architecture design of the UD. (**b**) Schematic of UD structure. (**c**)–(**e**) P_T, V_{OC}, I_{SC} of unit devices with different L_{ch} and W. (**f**) Critical width for device with different L_{ch}.

correlation between W_{th} and L_{ch}. Hereafter, we use $L_{ch} = 2$ μm and W = 10 μm to avoid unexpected V_{OC} drops to scale up the TMD-based Schottky-type solar cell.

To increase P_T, we attempted to connect multiple UDs in parallel. With the increasing number of parallel connections (N_{pa}) of UD, P_T increased up to $N_{pa} = 11$ (Fig. S6). However, a further increase in N_{pa} caused a sharp drop in V_{OC}, resulting in a lower P_T; this could also be explained by the aforementioned percolation model.

Once we found a suitable structure for UD and N_{pa}, the effect of the number of series connections (N_{se}) was investigated. When N_{se} was less than 4, P_T and V_{OC} increased (Fig. S7). When N_{se} was larger than 4, the P_T drop mainly came from the decrease in not only V_{OC} but also I_{SC}, implying an excessive carrier loss owing to the longer travelling distance of the carriers. It may happen the recombination of carrier when carrier density increase rather than the critical threshold. At current stage, we have not been able to conduct the recombination lifetime measurements, which will keep as one of the future works.

The combination of parallel and series connections, as well as further paralleling of UDM-B (unit device module C (UDM-C)) was also investigated. It was found that P_T increased by more than 10^6 times than that of UD upon repeatedly connecting 18,750 units of UDM-B at the cm-scale (Fig. 5a (i–ii) and 5b). As a control experiment, simply scaled up devices ($L_{ch} = 2$ μm and W = 3000 μm; all parallel connections) were fabricated, in which P_T did not increase even with a device area 10^6 times larger than that of UD (Fig. 5a (iii–iv) and b) (Fig. S8). These results indicate that the appropriate series–parallel composite design is of significant importance to P_T optimization of TMD-based NISCs.

Finally, a similarly optimized device designed on an SiO_2/Si substrate ((WO$_3$/Cu/ITO-ITO) and architecture (UDM-C: UD × 3 parallel connections (UDM-A) × 4 series connections (UDM-B) × 18,750 parallel connections)) were fabricated on a quartz substrate (Fig. 5c) (Fig. S9). As a result, the AVT and P_T reached up to 79% and 420 pW, respectively (Fig. 5d and e), which can drive several real devices[23]. To the best of our knowledge, this is the first investigation on realizing an NISC with TMD, and with the P_T obtained being the highest value for a solar cell using a monolayer or a few layers of TMD regardless of the AVT (Table S2).
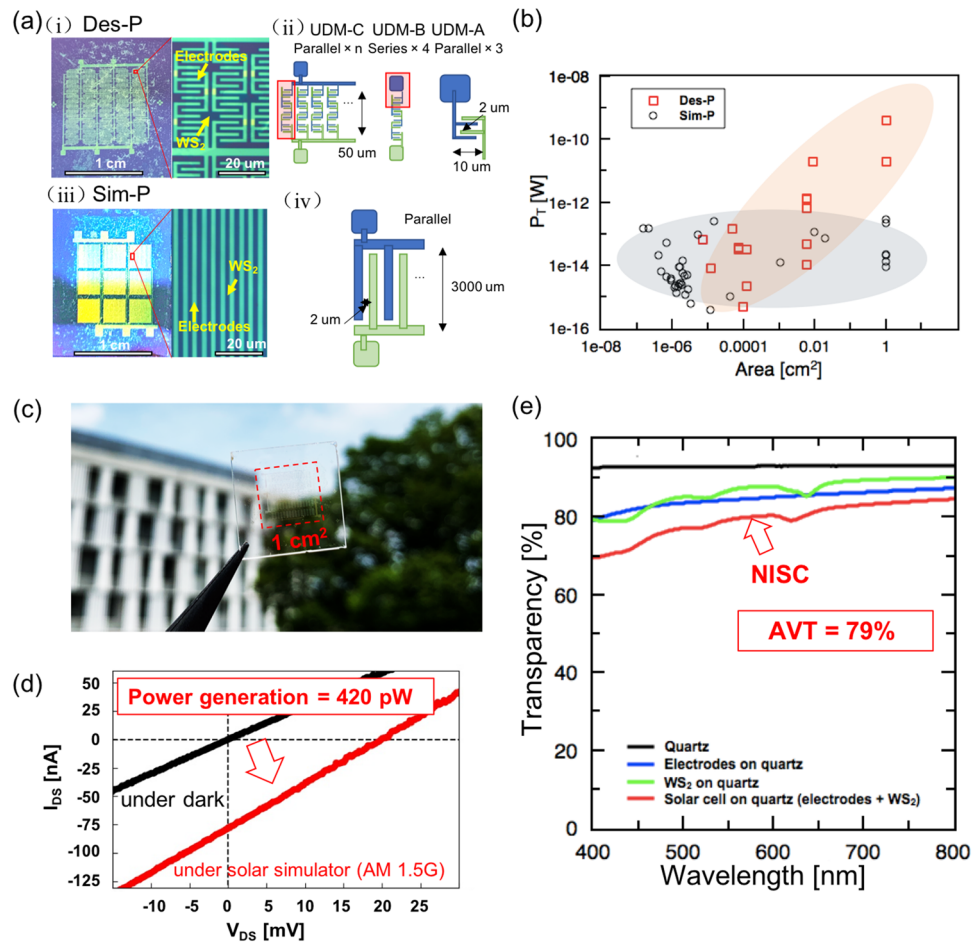
Figure 5. (**a**) (i) Image for solar cell with designed pattern (Des-P), (ii) structure diagram of designed pattern, (iii) image for solar cell with simple pattern (Sim-P), and (iv) structure diagram of simple pattern. (**b**) Plot of P_T for solar cells with different areas in Sim-P or Des-P. (**c**) Optical image of a highly transparent solar cell (**d**) I_{DS}-V_{DS} curve of highly transparent solar cell under dark or solar simulator. (**e**) Transmission of the NISC with comparison of WS$_2$ on quartz, electrodes on quartz, and pure quartz.

Conclusion

A monolayer WS$_2$ based NISC was successfully fabricated. The work function of the transparent ITO electrodes was modulated by a thin metal film coating without sacrificing the high transparency of ITO. A systematic investigation of Φ_B measurement with SPCM revealed that Φ_B was successfully controlled by the WF control of ITO and the S_F. A high Φ_B (~ 120 meV) was obtained using the Cu/ITO electrode. Φ_B could be further increased up to ~ 220 meV by inserting a thin film of WO$_3$ between the TMD and Cu/ITO electrode, and this can be explained by the reduced FLP effect. The PCE of the device with the highest Φ_B (WO$_3$/Cu/ITO) was more than 1000 times higher than that of the bare ITO electrodes. A suitable architectural design for large-scale device fabrication was also investigated. It was found that the aspect ratio (W/L$_{ch}$) of the TMD device should be lower than the critical value of approximately 36, which can be determined by the percolation model. By further scaling up the device size by considering an optimal series–parallel connection structure, an extremely high transparency of 79% could be realized, with P_T reaching up to 420 pW; this is the highest value within a TMD based solar cell with a few layers. These findings can contribute to the study of TMD-based NISCs from fundamentals to truly industrialized stages.

Experiment and method

Structural characterization of the TMD. The structures of the TMD were characterized by optical microscopy, Raman spectroscopy, and PL spectroscopy (LabRam HR800, HORIBA JOBIN YVON, Japan), and spatial mapping measurements with a 532-nm laser (Fig. S10).

Device fabrication on SiO$_2$/Si or quartz substrates. WS$_2$ was synthesized by thermal CVD using WO$_3$ as the tungsten source[38,39]. Ar was used as the carrier gas at a flow rate of 150–500 sccm. Sulfur (15 mg) was placed in a CVD oven, and WO$_3$ (9 mg) on a quartz boat was set 15 cm downstream from the center of the CVD furnace. NaCl (1.5 mg) was mixed with WO$_3$ to enhance evaporation. Then, conventional electron beam lithog-

raphy, microwave-plasma sputtering of ITO (Fig. S11), vacuum evaporation of metal or metal oxide, and lift-off were used to fabricate the symmetric and asymmetric devices. For the small-scale and large-scale suspended device fabrication, the CVD-grown WS_2 was covered with a water-soluble polymer and transferred to the asymmetric electrodes by a homemade transfer system with a micro positioner and microscope. The polymer was carefully removed by soaking it in water to obtain a suspended WS_2 device between the asymmetric electrodes on an SiO_2/Si substrate or a large transparent quartz substrate.

Work function analysis.　The work functions of Mx/ITO were measured by photoelectron yield spectroscopy (M20 KV-200, BUNKO-KEIKI, Japan)[40]. ITO (~40 nm) was sputtered on a quartz substrate; thereafter, thin metal films (1–5 nm) were prepared by thermal evaporation, which was the same as that used for device fabrication.

AVT measurement.　AVT was measured using UV–Vis-NIR spectroscopy (V-7200HK, JASCO, Japan) for vis-transparency measurements. AVT was calculated as $AVT = \frac{\int T(\lambda)P(\lambda)S(\lambda)d\lambda}{\int P(\lambda)S(\lambda)d\lambda}$, where λ is the wavelength; T is the transmission; P is the photopic response; and S is the solar photon flux (AM1.5G) for window applications, or 1 for other applications[1].

Solar cell performance measurements.　The I_{DS}–V_{DS} measurements were performed using a semiconductor parameter analyzer (HP 4155 C, Agilent, Japan) and a solar simulator (HAL-320, 300 W Xenon ramp with an AM1.5 filter, Asahi Spectra, Japan). The I_{DS}–V_{DS} curves for the estimation of accurate PCE were measured with a reverse-to-forward bias (−1 to 1 V_{DS}), 1-mV step size, and 20-ms dwell time; however, no difference in I_{DS}–V_{DS} curves was observed between the forward and reverse sweep directions. The power of the solar simulator (1000 W/m^2) was calibrated using an AIST-certified standard solar cell (AK-100, KONICA MINOLTA Inc., JAPAN). We used the total area of the suspended WS_2 between the two electrodes as the active area for the estimation of PCE in a small-scale device (~μm^2).

Schottky barrier height measurements.　The Schottky barrier height was measured using a homemade spatially resolved photoexcited charge-carrier mapping (SPCM) system. Line profile and mapping measurements of the photocurrent were performed using a homemade current probe system combined with a Raman and PL mapping measurement system (SPEX HR 640, HORIBA JOBIN YVON, Japan). The laser wavelength was 633 nm, and the spot size was ~1 μm (×100 objective).

References

1. Traverse, C. J., Pandey, R., Barr, M. C. & Lunt, R. R. Emergence of highly transparent photovoltaics for distributed applications. *Nat. Energy* **2**, 849–860 (2017).
2. Liu, G. *et al.* Ultraviolet-protective transparent photovoltaics based on lead-free double perovskites. *Sol. RRL* **4**, 1–8 (2020).
3. Betancur, R. *et al.* Transparent polymer solar cells employing a layered light-trapping architecture. *Nat. Photonics* **7**, 995–1000 (2013).
4. Song, Y., Chang, S., Gradecak, S. & Kong, J. Visibly-transparent organic solar cells on flexible substrates with all-graphene electrodes. *Adv. Energy Mater.* **6**, 1600847-1–8 (2016).
5. Zhang, G. *et al.* A nonfullerene semitransparent tandem organic solar cell with 10.5% power conversion efficiency. *Adv. Energy Mater.* **8**, 1800529-1–6 (2018).
6. Zhao, Y., Meek, G. A., Levine, B. G. & Lunt, R. R. Near-infrared harvesting transparent luminescent solar concentrators. *Adv. Opt. Mater.* **2**, 606–611 (2014).
7. Yang, C. *et al.* Ultraviolet and near-Infrared dual-band selective-harvesting transparent luminescent solar concentrators. *Adv. Energy Mater.* **11**, 203581-1–10 (2021).
8. Ban, D. K., Patel, M., Nguyen, T. T. & Kim, J. All-transparent oxide photovoltaics: AZO embedded ZnO/NiO/AgNW band selective high-speed electric power window. *Adv. Electron. Mater.* **5**, 1900348-1–8 (2019).
9. Naim, W. *et al.* Transparent and colorless dye-sensitized solar cells exceeding 75% average visible transmittance. *JACS Au* **1**, 409–426 (2021).
10. Li, M. Z. *et al.* Vacuum-deposited transparent organic photovoltaics for efficiently harvesting selective ultraviolet and near-infrared solar energy. *Sol. RRL* **5**, 2000564–1–11 (2021).
11. Britnell, L. *et al.* Strong light-matter interactions thin films. *Science* **340**, 1311–1315 (2013).
12. Jariwala, D., Davoyan, A. R., Wong, J. & Van der Atwater, H. A. Waals materials for atomically-thin photovoltaics: promise and outlook. *ACS Photonics* **4**, 2962–2970 (2017).
13. Groenendijk, D. J. *et al.* Photovoltaic and photothermoelectric effect in a double-gated WSe_2 device. *Nano Lett.* **14**, 5846–5852 (2014).
14. Pospischil, A., Furchi, M. M. & Mueller, T. Solar-energy conversion and light emission in an atomic monolayer p-n diode. *Nat. Nanotechnol.* **9**, 257–261 (2014).
15. Wi, S. *et al.* Enhancement of photovoltaic response in multilayer MoS_2 induced by plasma doping. *ACS Nano* **8**, 5270–5281 (2014).
16. Memaran, S. *et al.* Pronounced photovoltaic response from multilayered transition-metal dichalcogenides pn-junctions. *Nano Lett.* **15**, 7532–7538 (2015).
17. Nazif, N. K. *et al.* High-performance p-n junction transition metal dichalcogenide photovoltaic cells enabled by MoO_x doping and passivation. *Nano Lett.* **21**, 3443–3450 (2021).
18. Cho, A. J., Song, M. K., Kang, D. W. & Kwon, J. Y. Two-dimensional WSe_2/MoS_2 p-n heterojunction-based transparent photovoltaic cell and its performance enhancement by fluoropolymer passivation. *ACS Appl. Mater. Interfaces* **10**, 35972–35977 (2018).

19. Pawar, S. A. *et al.* Heterojunction solar cell based on n-MoS₂/p-InP. *Opt. Mater.* **86**, 576–581 (2018).
20. Wang, L. & Sambur, J. B. Efficient ultrathin liquid junction photovoltaics based on transition metal dichalcogenides. *Nano Lett.* **19**, 2960–2967 (2019).
21. Akama, T. *et al.* Schottky solar cell using few-layered transition metal dichalcogenides toward large-scale fabrication of semitrans-parent and flexible power generator. *Sci. Rep.* **7**, 11967–1–10 (2017).
22. Chatterjee, S. & Tarique, M. A 100-nW sensitive RF-to-DC CMOS rectifier for energy harvesting applications. *In Proceedings of the IEEE International Conference on VLSI Design* 557–558 (2016).
23. Aiello, O., Crovetti, P., Lin, L. & Alioto, M. A pW-power Hz-range oscillator operating with a 0.3–1.8-V unregulated supply. *IEEE J. Solid-State Circuits* **54**, 1487–1496 (2019).
24. Yamaguchi, H. *et al.* Spatially resolved photoexcited charge-carrier dynamics in phase-engineered monolayer MoS₂. *ACS Nano* **9**, 840–849 (2015).
25. Sotthewes, K. *et al.* Universal Fermi-level pinning in transition-metal dichalcogenides. *J. Phys. Chem. C* **123**, 5411–5420 (2019).
26. Kim, C. *et al.* Fermi level pinning at electrical metal contacts of monolayer molybdenum cichalcogenides. *ACS Nano* **11**, 1588–1596 (2017).
27. Farmanbar, M. & Brocks, G. First-principles study of van der Waals interactions and lattice mismatch at MoS₂/metal interfaces. *Phys. Rev. B* **93**, 085304–1–12 (2016).
28. Varnamkhasti, M. G. & Shahriaria, E. Improvement of performance and stability of polymer photovoltaic cells by WO₃/CuPc as anode buffer layers. *J. Eur. Opt. Soc.* **10**, 15028 (2015).
29. Kandasamy, S. A. *et al.* Hydrogen and hydrocarbon gas sensing performance of Pt/WO₃/SiC MROSiC devices. *Sensors Actuators, B Chem.* **111**, 111–112 (2005).
30. Raja, M. *et al.* Investigation of microstructural, optical and dc electrical properties of spin coated Al:WO₃ thin films for n-Al:WO₃/p-Si heterojunction diodes. *Optik (Stuttg).* **145**, 169 (2017).
31. Smyth, C. M. *et al.* Origins of Fermi Level Pinning between Tungsten Dichalcogenides (WS₂, WTe₂) and Bulk Metal Contacts: Interface Chemistry and Band Alignment. *J. Phys. Chem. C* **124**, 14550 (2020).
32. Meyer, J. T. *et al.* Transparent inverted organic light-emitting diodes with a tungsten oxide buffer layer. *Adv. Mater.* **20**, 3839 (2008).
33. Lin, Z. *et al.* Defect engineering of two-dimensional transition metal dichalcogenides. *2D Mater.* **3**, 022002–1–21(2016).
34. Wang, L., Li, Y., Gong, X., Thean, A. V. Y. & Liang, G. A physics-based compact model for transition-metal dichalcogenides transis-tors with the band-tail effect. *IEEE Electron Device Lett.* **39**, 761–764 (2018).
35. Wang, L., Thean, A. V. Y. & Liang, G. Percolation theory based statistical resistance model for resistive random access memory. *Appl. Phys. Lett.* **112**, 253505–1–5 (2018).
36. Stauffer, D. & Bunde, A. Introduction to percolation theory. 93–120 (Taylor and Francis, London, 1994).
37. Wang, L., Thean, A. V. Y. & Liang, G. A statistical Seebeck coefficient model based on percolation theory in two-dimensional disordered systems. *J. Appl. Phys.* **125**, 224302–1–6 (2019).
38. Li, C., Kameyama, T., Takahashi, T., Kaneko, T. & Kato, T. Nucleation dynamics of single crystal WS₂ from droplet precursors uncovered by in-situ monitoring. *Sci. Rep.* **9**, 12958–1–7 (2019).
39. Qiang, X. *et al.* Non-classical nucleation in vapor–liquid–solid growth of monolayer WS₂ revealed by in-situ monitoring chemical vapor deposition. *Sci. Rep.* **11**, 22285–1–9 (2021).
40. Tavkhelidze, A. *et al.* Fermi-Level Tuning of G-Doped Layers. *Nanomaterials* **11**, 505 (2021).

Acknowledgements

Author contributions

T.Kato. supervised this project and conceived and designed the experiments. H.X., Y.I., and T.Kato. performed the synthesis and characterization of WS₂. H.X. fabricated devices used in this study. H.X. and T.Kato. carried out measurements and analysis of Schottky barrier height and solar cell performance. H.X., T.K., and T.Kato. co-wrote the manuscript.

Competing interests

The authors declare no competing interests.

Additional information

Supplementary Information The online version contains supplementary material available at https://doi.org/10.1038/s41598-022-15352-x.

Correspondence and requests for materials should be addressed to T.K.

Reprints and permissions information is available at www.nature.com/reprints.

Publisher's note Springer Nature remains neutral with regard to jurisdictional claims in published maps and institutional affiliations.